

Wave Breaking Dissipation Observed with “SWIFT” Drifters

JIM THOMSON

Applied Physics Laboratory, University of Washington, Seattle, Washington

(Manuscript received 29 January 2012, in final form 25 May 2012)

ABSTRACT

Energy dissipation rates during ocean wave breaking are estimated from high-resolution profiles of turbulent velocities collected within 1 m of the surface. The velocity profiles are obtained from a pulse-coherent acoustic Doppler sonar on a wave-following platform, termed a Surface Wave Instrument Float with Tracking (SWIFT), and the dissipation rates are estimated from the structure function of the velocity profiles. The purpose of the SWIFT is to maintain a constant range to the time-varying surface and thereby observe the turbulence in breaking crests (i.e., above the mean still water level). The Lagrangian quality is also useful to prefilter wave orbital motions and mean currents from the velocity measurements, which are limited in magnitude by phase wrapping in the coherent Doppler processing. Field testing and examples from both offshore whitecaps and nearshore surf breaking are presented. Dissipation rates are elevated (up to $10^{-3} \text{ m}^2 \text{ s}^{-3}$) during strong breaking conditions, which are confirmed using surface videos recorded on board SWIFT. Although some velocity contamination is present from platform tilting and heaving, the structure of the velocity profiles is dominated by a turbulent cascade of eddies (i.e., the inertial subrange). The noise, or uncertainty, in the dissipation estimates is shown to be normally distributed and uncorrelated with platform motion. Aggregated SWIFT measurements are shown to be useful in mapping wave-breaking dissipation in space and time.

1. Introduction

The breaking of ocean surface waves generates strong turbulence and energy dissipation. In deep water, breaking participates in air-sea exchange and limits wave growth (Banner and Peregrine 1993; Melville 1996). In shallow water, breaking suspends sediment, forces currents, and drives coastal morphology (Battjes 1988). Although the mechanisms differ, both types of breaking are effective at dissipating wave energy in the form of turbulent kinetic energy (Herbers et al. 2000; Gemmrich and Farmer 1999).

Field observations of deep water breaking (i.e., whitecaps) have shown that the turbulent dissipation rate is a function of wave steepness and is correlated with wind stress (Terray et al. 1996; Gemmrich and Farmer 1999, 2004; Gerbi et al. 2009; Thomson et al. 2009; Gemmrich 2010). Field observations of shallow water breaking (i.e., surf) have shown that the turbulent

dissipation rate is a function of water depth and is correlated with the energy flux gradient of shoreward swell (Trowbridge and Elgar 2001; Bryan et al. 2003; Feddersen 2012). These observations typically are made using fixed instruments mounted below the mean (still) water level. Thus, it has been difficult to estimate turbulent dissipation rates near the time-varying wave surface. Recently, Gemmrich (2010) used up-looking Doppler sonars to estimate dissipation within breaking wave crests and found dissipation rates 10 times higher than those measured below the mean water level.

Here, the method of Gemmrich (2010) is adapted to wave-following reference frame using a new Lagrangian drifter. The drifter, which is termed a Surface Wave Instrument Float with Tracking (SWIFT), is designed to follow the time-varying free surface while collecting high-resolution profiles of turbulent velocity fluctuations. The velocity fluctuations are used to estimate the turbulence dissipation rate following Wiles et al. (2006). Thus, the SWIFT measurements can be used to estimate both wave spectra (from the drifter motions) and wave-breaking dissipation (from the Doppler velocity profiles). Previously, drifters have been used in the

Corresponding author address: J. Thomson, 1013 NE 40th St., Applied Physics Laboratory, University of Washington, Seattle, WA 98105.

E-mail: jthomson@apl.washington.edu

nearshore to observe currents (Schmidt et al. 2003; MacMahan et al. 2009), as well as particle dispersion (Spydell et al. 2007). Drifters also have been used in the open ocean to observe wave breaking and air-sea exchange (Graber et al. 2000; Pascal et al. 2011). In addition to a Lagrangian reference frame, drifters have the advantage of measurement in the absence of ship interference (e.g., wave reflections from the hull).

The SWIFT platform and raw data collection are presented in section 2. Then, processing methods for wave spectra and turbulent dissipation rates are described in section 3, with an emphasis on separating platform motion from turbulence. The processing steps are demonstrated with data from the following two field tests: (a) shallow water surf at the Field Research Facility (FRF) in Duck, North Carolina, and (b) deep water whitecaps on Lake Washington in Seattle, Washington. For each field deployment, the methods are compared between “bursts” with weak wave breaking and with strong wave breaking, as quantified by a breaking rate from surface video data. For the Lake Washington tests, an independent measurement of the wave-breaking turbulent dissipation rate at one point in the vertical profile is obtained using an acoustic Doppler velocimeter (ADV) on board the SWIFT. In section 4, all bursts are aggregated to examine overall patterns in wave-breaking dissipation during the field testing. Discussion of the test results and data quality follow in section 5, and conclusions are given in section 6.

2. Measurements

SWIFT is shown in Fig. 1. The purpose of the SWIFT is to make measurements in a wave-following reference frame. The primary dimensions are a 2.15-m length overall (1.25-m draft + 0.9-m mast) and a 0.3-m-diameter hull. Onboard instruments include a GPS logger (QStarz BT-Q1000eX), a pulse-coherent Doppler velocity profiler [Nortek Aquadopp (AQD) HR], an autonomous meteorological station (Kestrel 4500), and a digital video recorder (GoPro Hero). The SWIFT location is tracked in real time with a radio frequency transmitter (Garmin Astro). SWIFT missions typically last several hours up to a full day, and data are collected in 5-min bursts. Upgrades are ongoing to swift including extending mission life, and integrating an ultrasonic anemometer (AirMar PB200) and data telemetry (Iridium).

A series of field tests have been conducted to refine the SWIFT design and data processing algorithms. To date, six SWIFTS have been fabricated and approximately 1300 h of SWIFT data have been collected.

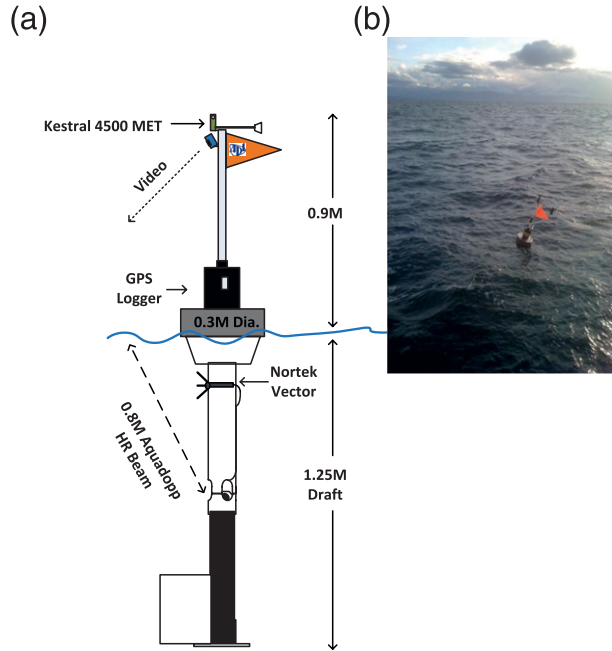


FIG. 1. (a) Dimensional drawing and (b) picture of a SWIFT. Drawing and design by J. Talbert, Applied Physics Laboratory, University of Washington.

Select data and results from tests are used to demonstrate the data collection and processing steps. For each field test, individual burst data and processing are compared between weak and strong breaking conditions (as determined from the onboard video recordings), and then patterns from aggregate results using all bursts are examined.

First, a shallow water test deployment was conducted over 4 h on 15 September 2010 at the U.S. Army Corps of Engineers (ACE) Field Research Facility in Duck. Conditions, as measured by FRF instruments, were onshore $2\text{--}5 \text{ m s}^{-1}$ winds and 10-s period swell, with 0.6-m significant wave height. The FRF uses a local coordinate system, in which x is increasing offshore and y is increasing alongshore. For these mild conditions and neap tides, the surf zone was contained with $75 < x < 175$ m. SWIFTS were released from a small boat outside of the surf zone (cross-shore distance $x \sim 250$ m, water depth $h \sim 4$ m) and were allowed to drift into the surf zone. SWIFTS eventually grounded on the beach and were recovered there. An early version of the SWIFT was used, which differed slightly from the version in Fig. 1. The earlier version used a 90° transducer head on the Aquadopp HR, which was mounted across the lower hull to achieve approximately the same beam geometry as the version in Fig. 1.

Second, a deep water test deployment was conducted over 6 h on 12 November 2011 on Lake Washington in

Seattle. Conditions, as measured by nearby meteorological station (King County buoy) and a Datawell Waverider buoy, were southerly 8–10 m s⁻¹ winds and 3-s-period fetch-limited waves, with 0–1-m significant wave height. The wave age was approximately $c_p/U_{10} = 0.4$, where c_p is the deep water phase speed and U_{10} is the wind speed at a 10-m reference height. SWIFTs were released from a small boat just north of the I-90 floating bridge in the middle of the lake and allowed to drift north along a fetch distance x , where $x = 0$ is the location of the floating bridge. SWIFTs were in deep water ($h > 30$ m) at all times, as confirmed via postprocessing of GPS positions with bathymetry in Google Earth. As shown in Fig. 1, this version of SWIFT included an acoustic Doppler velocimeter [Nortek Vector (VEC)] sampling at a single bin in the middle of the Aquadopp HR profile.

a. Platform motion

The SWIFT wave-following motion is measured via GPS logger (QStarz BT-Q1000eX) at 5 Hz, following Herbers et al. (2012). Although the absolute horizontal accuracy of the differential GPS (DGPS) positions is only 10 m, the relative horizontal velocity resolution is much higher (0.05 m s⁻¹) and suitable for the orbital motions of most ocean waves. This velocity resolution is possible by Doppler phase processing the raw GPS signals. The GPS vertical elevation accuracy is not sufficient to track wave-following motion; however, relative (i.e., in the wave-following reference frame) vertical information is available from the pressure and orientation sensors in the Nortek Aquadopp HR. The Aquadopp pressure is equivalent to the SWIFT surface tracking, and pitch and roll are equivalent to the components of the SWIFT vertical tilting. (Constant values from these sensors indicate good wave-following behavior.) The GPS and Aquadopp orientation data are processed to determine the wave-height spectra and the quality of wave following, respectively.

In addition to wave-following motions, the SWIFT oscillates, or “bobs,” at a natural frequency. The SWIFT has 12.7-kg buoyancy in the main hull (0.3-m diameter, see Fig. 1) and 2.6 kg of lead ballast at the bottom of the lower hull (i.e., 1.25 m below the surface). Following Middleton et al. (1977), the corresponding theoretical natural period is $T_n \approx 1.3$ s, which is intentionally shorter than most ocean waves. This natural oscillation is damped by a heave plate at the bottom of the lower hull (see Fig. 1).

While wave following, the SWIFT also drifts with mean currents and wind. Tests in Puget Sound, under a range of tidal currents from 0.4 to 2.2 m s⁻¹, indicate drift velocities are consistent with fixed ADCP

observations (not shown). Wind drag causes the SWIFTs to drift with the wind, which is measured on board the SWIFT at 0.9 m above the surface, at about 5% of the wind speed (as empirically determined from tests in 0–14 m s⁻¹ winds). While drifting, a subsurface vane on the lower hull (see Fig. 1) provides additional drag to maintain an orientation such that the video and Aquadopp beam 1 look upwind (or upwave, for locally generated wind waves). Under strong winds, the drag of the 0.9-m mast causes a steady tilt of the SWIFT relative to the vertical of approximately 5°–10° (see picture in Fig. 1). This mean tilt changes slightly the vertical projection of subsurface velocity profiles (next section), but otherwise has negligible effects.

b. Turbulence profiles $u'(z)$

Turbulent velocity profiles $u'(z)$ are obtained with a 2-MHz Nortek Aquadopp HR (pulse coherent) Doppler profiler, where z is the distance below the wave-following surface at $z = 0$. The Lagrangian quality of the drifter is motivated, in part, by range and magnitude limitations in the Doppler measurements of $u'(z)$ and the goal of measuring turbulence within the crests of breaking waves (i.e., above the still water level). The Aquadopp is mounted in the lower hull and collects along-beam velocity profiles at 4 Hz with 0.04-m vertical resolution along a 0.8-m beam. Bursts of 1024 profiles (=256 s) are collected at 300-s intervals. The beam is orientated up- and outward at an angle of $\bar{\theta} = 25^\circ$ relative to vertical (see Fig. 1), and the SWIFT is vaned to keep this beam looking upwave (to avoid measuring the drift wake of the SWIFT). In field testing, wave reflections from the main hull of SWIFT are not observed, presumably because the SWIFT is moving with the free surface. The blanking distance next to the transducer is 0.1 m, and thus the actual beam profile is 0.7 m long.

The along-beam velocities are mapped, but not projected, to a vertical coordinate z for subsequent processing and plotting (i.e., each value of u' is unchanged, but is assigned a z location). The z location is defined as the distance beneath the instantaneous free surface ($z = 0$) and the Aquadopp pressure gauge (also sampled a 4 Hz) is used to correct for any changes in the water-line level at the SWIFT. This correction is small (a result of the wave-following nature of the platform), and never shifts the observed profile up or down more than one profile bin (i.e., ± 0.04 m).

Figure 2 show examples of raw Aquadopp data for selects bursts (4 Hz for 5 min) from outside and inside of the surf zone at Duck (left versus right panels). Figure 3 shows examples of raw Aquadopp data for selects bursts with mild breaking at short fetch and

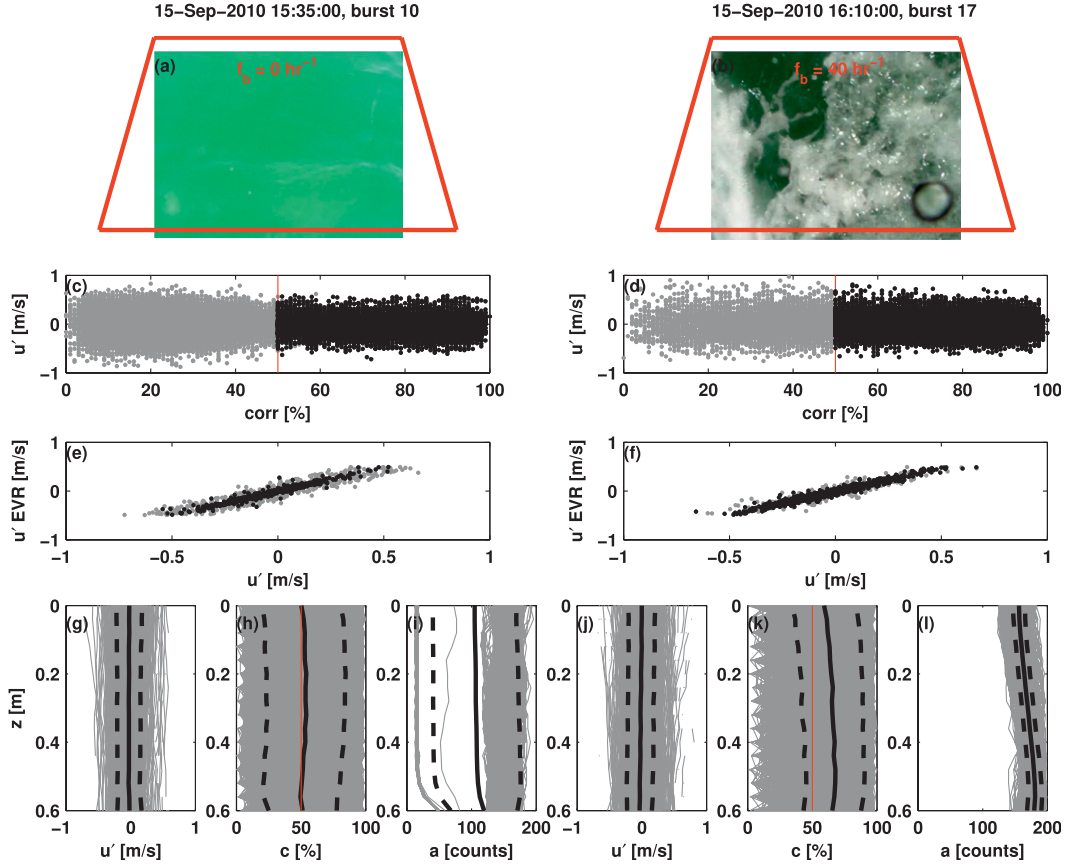


FIG. 2. Example raw SWIFT burst data collected in shallow water at the Duck FRF. (left) Nonbreaking conditions outside of the surf zone, and (right) breaking conditions within the surf zone are shown. (a),(b) Onboard video images with rectified 1-m² regions for counting breakers (red outline). (c),(d) Quality-controlled velocity data using a pulse-to-pulse correlation cutoff $c > 50$ (red lines). (e),(f) Comparisons of extended velocity range measurements with midprofile velocity measurements. (g),(j) Vertical profiles of turbulent velocity $u'(z)$. (h),(k) Vertical profiles of correlation $c(z)$. (i),(l) Vertical profiles of backscatter amplitude $a(z)$. Mean values (thick black lines) and \pm one standard deviation (dashed black lines) are shown.

strong breaking at long fetch (left versus right panels). The surface elevation ($z = 0$) appears constant in the lower panels because the SWIFT is following the free surface. The depth profiles of $u'(z)$ do not show any strong trends. However, in shallow water, the backscatter amplitude is uniformly increased in the surf zone example ($a \sim 200$ counts, Fig. 2l) compared with the offshore example ($a \sim 150$ counts, Fig. 2i), consistent with the presence of bubbles in the surf zone. In deep water, the amplitude increases slightly near the surface for both examples (Figs. 3i,l), consistent with bubble injection by wave breaking (whitecaps).

A major concern with up-looking Doppler measurements is interference from surface reflections. This is especially significant for coherent systems. Profiles of along-beam backscatter amplitude and coherence (e.g., Figs. 2h–l and 3h–l) are used to look for interference, which would appear as a peak in amplitude and

reduction in coherence at specific location in the profile (corresponding to a returning pulse interfering with an outgoing pulse). These and other profiles of amplitude and correlation do not show any sharp features that would indicate interference from surface reflections. Using a pulse distance of 0.8 m, which is similar to actual distance to the surface, is the minimum value that can be used.

The velocity data are quality controlled using a minimum pulse correlation value of $c > 50$ (out of 100) and a minimum backscatter amplitude $a > 30$ counts, which were empirically determined to be the maximum values associated with spurious points and with bins out of the water. Nortek notes that a canonical value of $c > 70$ is often overly restrictive, and recommends $c > 50$ as a more useful cutoff (Rusello 2009). For ADV measurements, an accepted threshold is $c > 30 + 40\sqrt{f_s/f_{\max}}$, where f_s and f_{\max} are the actual and maximum possible

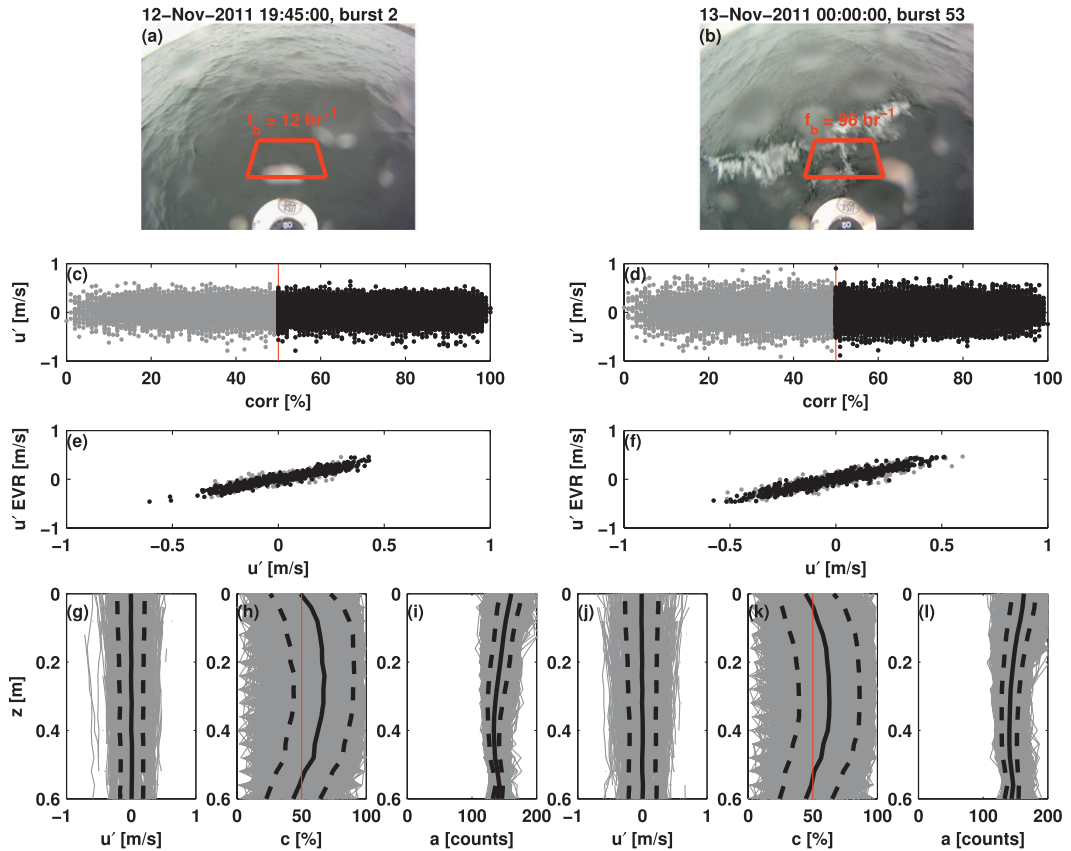


FIG. 3. Example raw SWIFT burst data collected in deep water on Lake Washington. (left) Moderate breaking conditions at a short fetch distance, and (right) strong breaking conditions at a larger fetch distance. (a),(b) Onboard video images with rectified 1 m^2 regions for counting breakers (red outlines). (c),(d) Quality-controlled velocity data using a pulse-to-pulse correlation cutoff $c < 50$ (red lines). (e),(f) Comparisons of extended velocity range measurements with midprofile velocity measurements. (g),(j) Vertical profiles of turbulent velocity $u'(z)$. (h),(k) Vertical profiles of correlation $c(z)$. (i),(l) Vertical profiles of backscatter amplitude $a(z)$. Mean values (thick black lines) and \pm one standard deviation (dashed black lines) are shown.

sampling frequencies, respectively (Elgar et al. 2001; Feddersen 2010). Although ADVs are point measurements, instead of profile measurements, ADVs operate on the same coherent processing between pulse pairs to determine the Doppler shift, and thus velocity. Applying the threshold here, using $f_s = 4 \text{ Hz}$ and $f_{\max} = 8 \text{ Hz}$, gives a threshold of $c > 58$, similar to the ad hoc choice of $c > 50$. This choice of correlation cutoff is evaluated in section 5 by comparing the sensitivity of results obtained in postprocessing with cutoff values of $c > 0, 25, 50$, and 75 .

For the Duck measurements shown in Fig. 2, there is a notable decrease in scatter for velocity measurements above the chosen correlation cutoff $c > 50$ (Figs. 2c,d). For the Lake Washington measurements shown in Fig. 3, the scatter for velocity measurements is similar above and below the chosen correlation cutoff $c > 50$ (Figs. 3c,d). Observations with $c > 50$ or $a < 30$ are assigned NaN

velocity values and ignored during subsequent analysis (i.e., no interpolation). At worst, the quality control ratio of points removed to total points is 1:2, or half of the data in a given burst. At Duck, the burst data outside of the surf zone include a brief period ($\sim 20 \text{ s}$) with the instrument out of the water for repositioning, and this results in a much higher quality control ratio (i.e., more points are removed from the velocity data prior to processing). Even in these cases with significant data removal, there are at least 512 profiles remaining with which to determine the average structure of the turbulence. More often, the quality control ratio is less than 1:10.

The velocity data also are quality controlled by examining the extended velocity range (EVR) data in the HR mode, which uses a second, shorter pulse lag to obtain a wider velocity range at point in the middle of the profile ($z = 0.3 \text{ m}$). Here, the pulse distances are 0.8

and 0.26 m, and the along-beam velocity range is 0.5 m s^{-1} . Comparing the profile and EVR data is essential to confirm that phase wrapping has not occurred. Comparing the profile and EVR data also is useful to evaluate quality control via coherence and amplitude thresholds (i.e., for data within the velocity range, points with low correlations c or amplitudes a should be the only points that do not compare well). For the Duck measurements shown in Fig. 2, there is improved agreement between the profile data and the EVR data for velocity measurements above the chosen correlation cutoff $c > 50$ (Figs. 2e,f). For the Lake Washington measurements shown in Fig. 3, there is no significant difference in the EVR agreement for quality-controlled data (Figs. 3e,f).

The pulse-coherent measurements from the Aquadopp HR do not have a nominal Doppler uncertainty, or “noise,” value. Zedel et al. (1996) show that noise is a function of the coherence of each pulse pair, as well as sampling parameters (i.e., rate, number of bins) that control Doppler phase resolution. Still, a nominal value is useful when interpreting results. Here, a nominal velocity uncertainty (standard error) of $\sigma_u = 0.025 \text{ m s}^{-1}$ is applied, which is 5% of the along-beam velocity range and similar to the $\sigma_u = 0.02 \text{ m s}^{-1}$ reported by Zedel et al. (1996) for a correlation $c = 50$. Because this is the minimum correlation used, the actual σ_u of a burst is likely to be less than this. This noise is large compared with more common measurements of turbulent flows; however, the noise can be isolated in the processing of turbulent spatial structures. In practice, the noise is not prescribed, but rather is retained as a free parameter in the solution for the dissipation rate (section 3c). This empirical noise is later compared with the nominal variance of σ_u^2 to evaluate results (section 5).

c. Surface images

Time-lapse images of the surface are collected at 1 Hz from a GoPro Hero camera mounted to the mast at an elevation of 0.8 m above the surface and an incidence angle of 35° relative to nadir. Recording in mode “r4,” the horizontal field of view is 170° and the images are 2592×1944 pixels. Example images are shown in Figs. 3a,b. The shallow water testing at the FRF used a ruggedized Sanyo video camera recording at 30 Hz with a much reduced field of view, as shown in Figs. 2a,b. The images are processed to estimate the frequency of wave breaking f_b , which is used as context for the turbulent dissipation rate estimates.

3. Methods

The SWIFT drifters are designed to make in situ observations of velocity u that can be decomposed as

$$u = \bar{u} + \tilde{u} + u', \quad (1)$$

where \bar{u} is the time mean drift velocity measured by the changing GPS positions, \tilde{u} are the wave orbital velocities measured by the phase-resolving GPS velocities, and u' are the turbulent fluctuations of velocity measured by the Aquadopp HR. The mean and wave orbital velocities are measured at the surface ($z = 0$) as horizontal vectors in the earth reference frame, and the turbulent fluctuations are measured as depth profiles $u'(z)$ of scalar along-beam components in the wave-following reference frame. SWIFT data are parsed into 5-min bursts for processing, and the angle bracket ($\langle \rangle$) notation will be used to denote burst ensembles. Overbars will be used for burst-averaged quantities. For example, the SWIFT GPS velocities are averaged to determine the mean drift velocity $\bar{u} = \langle u \rangle$. These bursts are sufficiently short to have quasi-stationary statistics (i.e., steady mean and variance), but long enough to have meaningful confidence intervals on calculated quantities. Given a typical drift speed of $\bar{u} \sim 0.2 \text{ m s}^{-1}$, a SWIFT drifts approximately 60 m during a burst. The burst-averaged quantities must assume homogeneity over this scale, which may be a poor assumption in a region of rapidly evolving waves (e.g., the surf zone).

The wave-following behavior of the SWIFTS, which separates wave orbital velocities \tilde{u} from turbulent fluctuations u' , is essential to the estimates of wave spectra and turbulent dissipation rates, respectively. These quantities, and the quality of wave following, are described in the following subsections.

a. Frequency spectra $S(f)$

Frequency spectra $S(f)$ are used to evaluate the motion of the SWIFT and to quantify the wave conditions. Spectra for each 5-min burst are calculated as the ensemble average of the fast Fourier transform (FFT) of 16 subwindows with 50% overlap, which resulting in 32 degrees of freedom and a frequency bandwidth $df = 6.25 \times 10^{-2} \text{ Hz}$. Figures 4 and 5 show example spectra from Duck and Lake Washington, respectively, using the same example bursts (showing weak and strong wave breaking) discussed in the previous section (section 2).

Spectra from Aquadopp orientation data (i.e., pitch, roll, and heading), $S_{\theta\theta}(f)$, are used to assess the tilting and turning of the SWIFT during wave following. In Figs. 4a and 5a, example orientation spectra $S_{\theta\theta}(f)$ show broad peaks at the natural period of the platform and at the period of the waves. The weak response at wind sea frequencies (0.4–0.5 Hz) indicates some rotation and tilting during wave following. However, the more

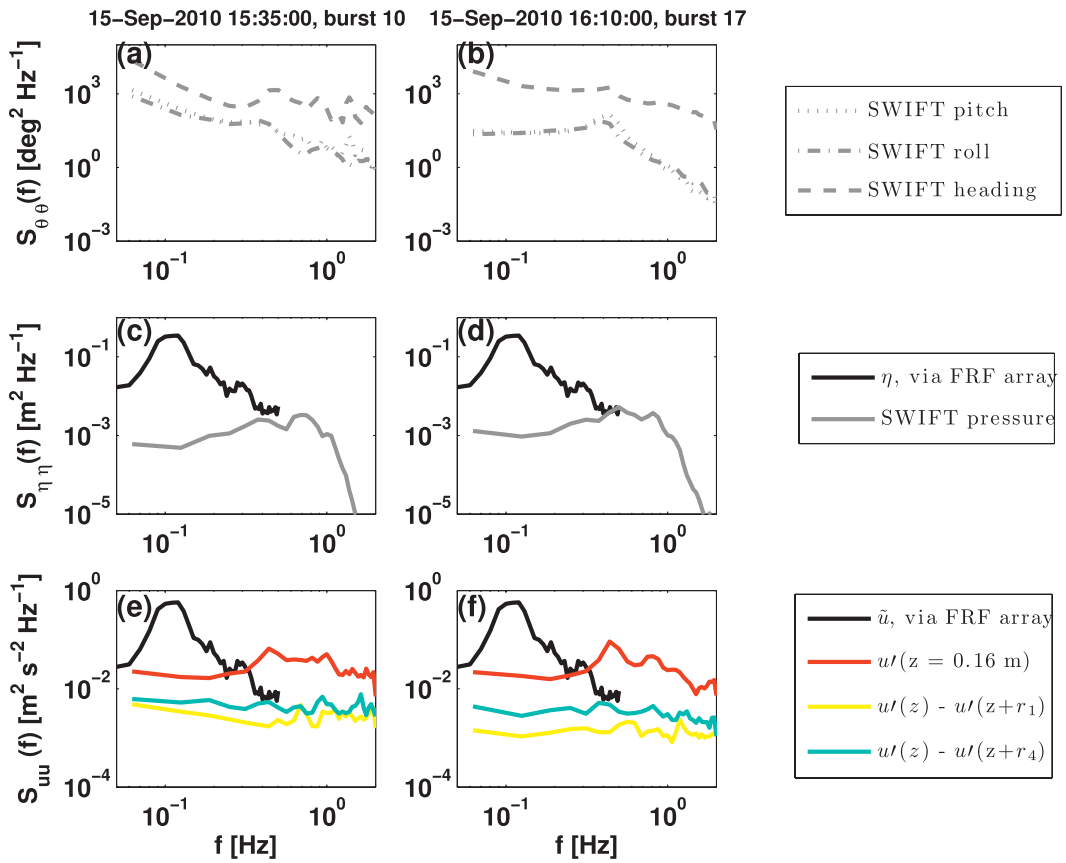


FIG. 4. Example frequency spectra calculated from burst data in shallow water at the Duck FRF. (left) Non-breaking conditions outside of the surf zone, and (right) breaking conditions within the surf zone. (a),(b) SWIFT platform orientation spectra (pitch, roll, and heading). (c),(d) Wave energy spectra (from independent FRF measurements) and SWIFT pressure spectra (from the Aquadopp). (e),(f) Velocity spectra, including wave orbital motion (from independent FRF measurements), SWIFT turbulence at one selected vertical position, and turbulence difference between selected vertical positions.

prominent signals are the trends caused by shifting winds and surface currents (i.e., low frequencies). These platform motions shift the entire Aquadopp profile $u'(z)$ with an offset Δu_θ , which has a negligible effect on the structure of $u'(z) - u'(z + r)$.

Spectra from the Aquadopp pressure data (i.e., relative distance below the surface), $S_{pp}(f)$ are used to assess the surface tracking of the SWIFT during wave following. In Figs. 4b and 5b, the natural frequency (~ 0.7 Hz) is the dominant peak in the pressure spectra $S_{pp}(f)$, and wave peaks are negligible (i.e., pressure fluctuations from waves are absent in the wave-following reference frame). Integrating $S_{pp}(f)$ around the natural frequency estimates the variance in the surface tracking owing to bobbing of the platform. In field testing, this variance is typically $O(10^{-4} \text{ m}^2)$, or a vertical standard deviation of $\sigma_z \sim 0.01$ m.

In contrast, the SWIFT horizontal velocity data from the phase-resolving GPS contain the wave orbital

motions relative to the earth reference frame. Following Herbers et al. (2012), the wave orbital velocity spectra $\int S_{\tilde{u}\tilde{u}}(f) df = \langle (u - \bar{u})^2 \rangle$ is used to estimate the underlying wave conditions. The scalar wave-height spectra $S_{\eta\eta}(f)$ can be calculated from $S_{\tilde{u}\tilde{u}}$ using linear finite-depth theory (Mei 1989), if the water depth is known from another source. In deep water, the conversion is simply $S_{\eta\eta}(f) = S_{\tilde{u}\tilde{u}}(f)(2\pi f)^{-2}$. In practice, this is done component-wise, with the total scalar spectrum equal to the sum of the converted spectrum of the two orthogonal velocity components. For the Duck testing, SWIFT GPS data were not of sufficient quality to estimate wave spectra, and wave spectra from a nearby FRF array instrument (an Aquadopp at $x = 232$ m) are used. For the Lake Washington testing, SWIFT wave spectra $S_{\eta\eta}(f)$ are consistent with nearby Datawell Waverider measurements of wind waves with a peak frequency of $f = 0.3$ Hz. The SWIFT wave spectra also exhibit the expected $S_{\eta\eta}(f) \sim f^{-4}$ equilibrium range at frequencies greater

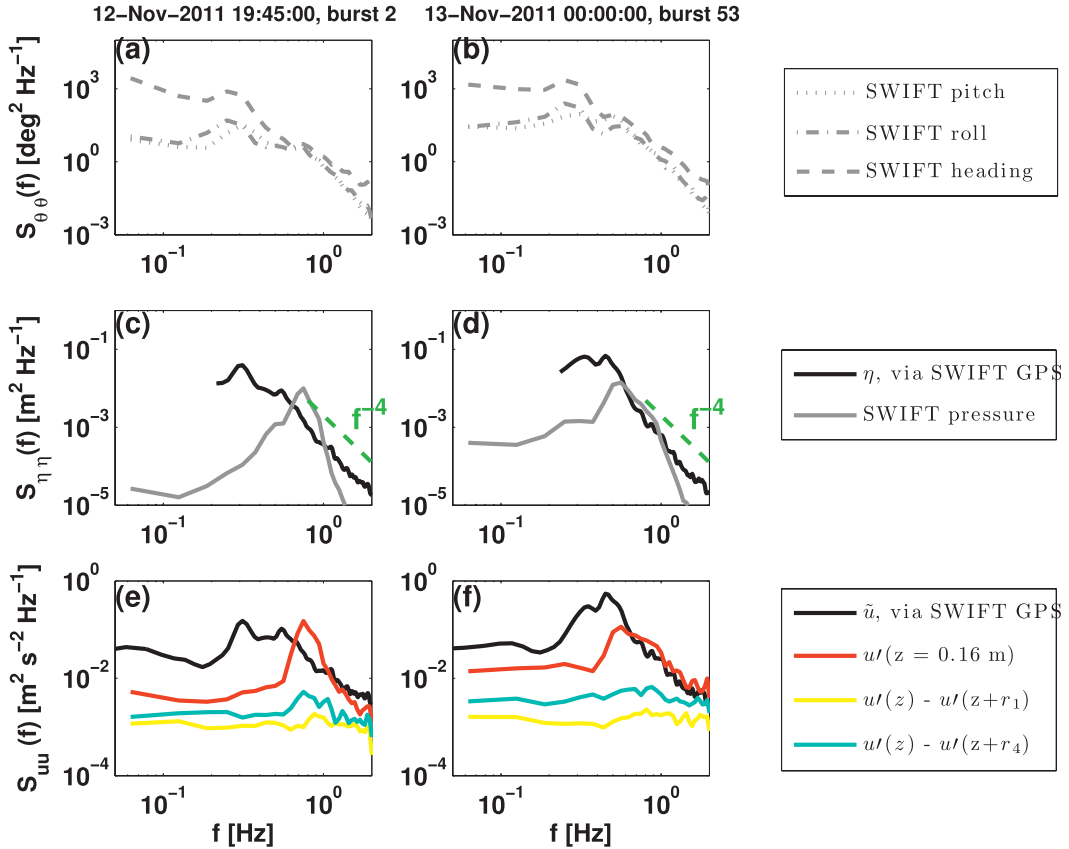


FIG. 5. Example frequency spectra calculated from burst data in deep water on Lake Washington. (left) Moderate breaking conditions at a short fetch distance, and (right) strong breaking conditions at a larger fetch distance. (a),(b) SWIFT platform orientation spectra (pitch, roll, and heading). (c),(d) Wave energy spectra (from SWIFT GPS measurements) and SWIFT pressure spectra (from the Aquadopp). The theoretical equilibrium range is shown (green dashed lines). (e),(f) Velocity spectra, including wave orbital motion (from SWIFT GPS measurements), SWIFT turbulence at one selected vertical position, and turbulence difference between selected vertical positions.

than the peak (Figs. 5c,d). This suggests that SWIFT observations can be used to study waves ranging from low-frequency swell to high-frequency wind seas, because oscillations at the natural frequency of the platform $S_{pp}(f)$ do not have significant effect on the fidelity of the platform to track horizontally with the wave orbital velocities [and thereby obtain $S_{\eta\eta}(f)$, similar to Herbers et al. (2012)].

Finally, spectra of the Doppler turbulent velocity profiles $S_{u'u'}(f)$ are used to look for contamination from SWIFT motion. Even for perfect wave following, the $S_{u'u'}(f)$ spectra will have a peak at the natural frequency of the SWIFT, similar to the pressure spectra. For cases with significant tilt and rotation contamination, the $S_{u'u'}(f)$ spectra may have a peak at wave orbital frequencies as well. Figures 4e,f and 5e,f suggest both sources of contamination are present. The relevant quantity for estimating turbulent dissipation, however, is the difference between points in the velocity profile $u'(z) - u'(z + r)$.

The velocity differences (i.e., the turbulence) along a profile are much less susceptible to motion contamination, because platform motion contaminates the entire profile (i.e., an offset). Thus, spectra of velocity differences at selected points along the profile are used to evaluate the motion contamination for the purpose of turbulence calculations. Figures 4c and 5c show spectra two selected velocity differences (between depths $[z, z + r_1]$ and $[z, z + r_4]$) for the example bursts, and the velocity difference spectra all lack the peaks associated with motion contamination. Moreover, the velocity difference spectra show an expected increase in energy density between smaller ($r_1 = 0.4$ m) and larger ($r_4 = 0.16$ m) lag distances (i.e., eddy scales), consistent with a turbulent cascade.

b. Turbulence structure function $D(z, r)$

The along-beam Doppler velocity profiles $u'(z)$ are processed to estimate the turbulent dissipation rate following the method of Wiles et al. (2006), in which the

vertical second-order structure function $D(z, r)$ of velocity fluctuations $u'(z)$ is defined as

$$D(z, r) = \langle [u'(z) - u'(z + r)]^2 \rangle, \quad (2)$$

where z is the vertical location beneath the free surface, r is the along-beam lag distance between velocity measurements, and the angle bracket denotes the burst time average (5 min). This choice of time scale obscures the details of individual breaking events in favor of robust statistics on the overall effect of breaking (enhanced turbulent dissipation near the free surface). Note that variance in time is not significant to the structure function, other than as contamination by nonstationarity, because it is the difference of $u'(z)$ over spatial scales r that controls $D(z, r)$. The lag distances r are limited to half of the profile length or the distance to the boundary, whichever is smaller. As shown by Gemmrich (2010), estimation of the structure function beneath breaking waves is sensitive to the maximum separation scale $|r|$ used, because turbulence may decay rapidly beneath the wave crests (i.e., heterogeneity).

The $D(z, r)$ is one sided, such that differences are taken from the top of the profile downward, which is necessary to correct for platform motion. Platform motion contaminates estimates of $D(z, r)$ by causing overlap in along-beam velocity measurements. When the SWIFT heaves (i.e., bobs) relative to the wave-following surface, neighboring velocity bins are no longer fully independent, because the heaving motion moves the instrument relative to the bins. Similarly, when the SWIFT tilts, the projection of velocity bins shifts, and neighboring velocity bins overlap. The overlap will reduce the velocity differences in Eq. (2) and thus bias low the estimates of $D(z, r)$. The bias can be removed by applying a correction to the lag distances $r = r_0 - \Delta r$, such that

$$r = r_0 - \left(\frac{\sigma_z}{\cos \bar{\theta}} \right) - \left[\frac{z_0 - z}{2 \cos^2 \bar{\theta}} (\bar{\theta} \sigma_\theta) \right], \quad (3)$$

where the first term is the original lag distance r_0 , the second term is the correction for heave in vertical position z , and the third term is the correction for tilting in the beam angle θ . Corrections are made using the measured deviations from perfect wave-following motion: σ_z is the standard deviation of the Aquadopp distance z_0 beneath the wave-following surface (measured by the onboard pressure gauge) and σ_θ is the standard deviation of beam angle θ in radians (inferred from the onboard orientation sensor). Using typical values of $\sigma_z = 0.01$ m and $\sigma_\theta = 0.09$ rad ($=5^\circ$), the typical

correction is $\Delta r \sim 0.03$ m, which is small relative to the $\mathcal{O}(0.5)$ m lag distances used to determine $D(z, r)$. Finally, it must be noted that the triangular bin weighting used in Nortek's processing also results in some overlap in velocity information between neighboring bins, but that offset is not treated by Eq. (3).

Figures 6 and 7 show examples of the structure functions $D(z, r)$ calculated outside and inside of the surf zone (Fig. 6a versus Fig. 6b) and during mild and strong whitecapping (Fig. 7a versus Fig. 7b). In each example, there are trends for increased velocity differences with increasing lag distances r , and the slopes of these trends differ by vertical location beneath the wave-following surface (color scale of z in the figures). These trends are consistent with a cascade of turbulent kinetic energy from large to small eddies.

In terms of wavenumber k , the energy in a cascade of isotropic eddies is expected to follow a $k^{-5/3}$ dependence (Kolmogorov 1941), which is often observed indirectly as a frequency $f^{-5/3}$ dependence via application of Taylor's frozen field hypothesis. Here, the spatial structure of the turbulence is interpreted as a direct observation of the energy cascade that follows a power law $D(z, r) \sim u'^2 \sim r^{2/3}$ (equivalent to $k^{-5/3}$). The burst estimates of $D(z, r)$ are fit to a linear model

$$D(z, r) = A(z)r^{2/3} + N, \quad (4)$$

where an A is determined for each z using MATLAB's robust fit algorithm and N is an offset resulting from measurement noise. Examples of the $A(z)r^{2/3}$ fit are shown in Figs. 6a,b and 7a,b, where the slopes $A(z)$ increase near the surface ($z = 0$) and during strong breaking (Figs. 6b and 7b). The slopes $A(z)$ are used to estimate the rate at which turbulent kinetic energy is dissipated (next section). The correlation coefficients for these examples are greater than 0.8 at all level z levels, which is typical over all test bursts (not shown).

The offset N is expected to be $2\sigma_{u'}^2$, in which $\sigma_{u'}$ is the Doppler noise of the velocity measurement (Wiles et al. 2006; Rusello and Cowen 2011). The Doppler noise contributes additional differences between velocity measurements uniformly across all lag distances, and thus will produce a positive offset to $D(z, r)$. Here, N values are obtained as a free parameter in the fits (rather than prescribed) and are used to evaluate errors in the methods or violations in the assumptions (see section 5). In the examples, the noise intercepts N are similar or less than the predicted $2\sigma_{u'}^2$ value, which is shown by an open triangle on the vertical axis of Figs. 6a,b and 7a,b. The N values are used for quality control, by accepting only $N < 2\sigma_{u'}^2$ and $N \ll Ar^{2/3}$. The noise intercepts also are

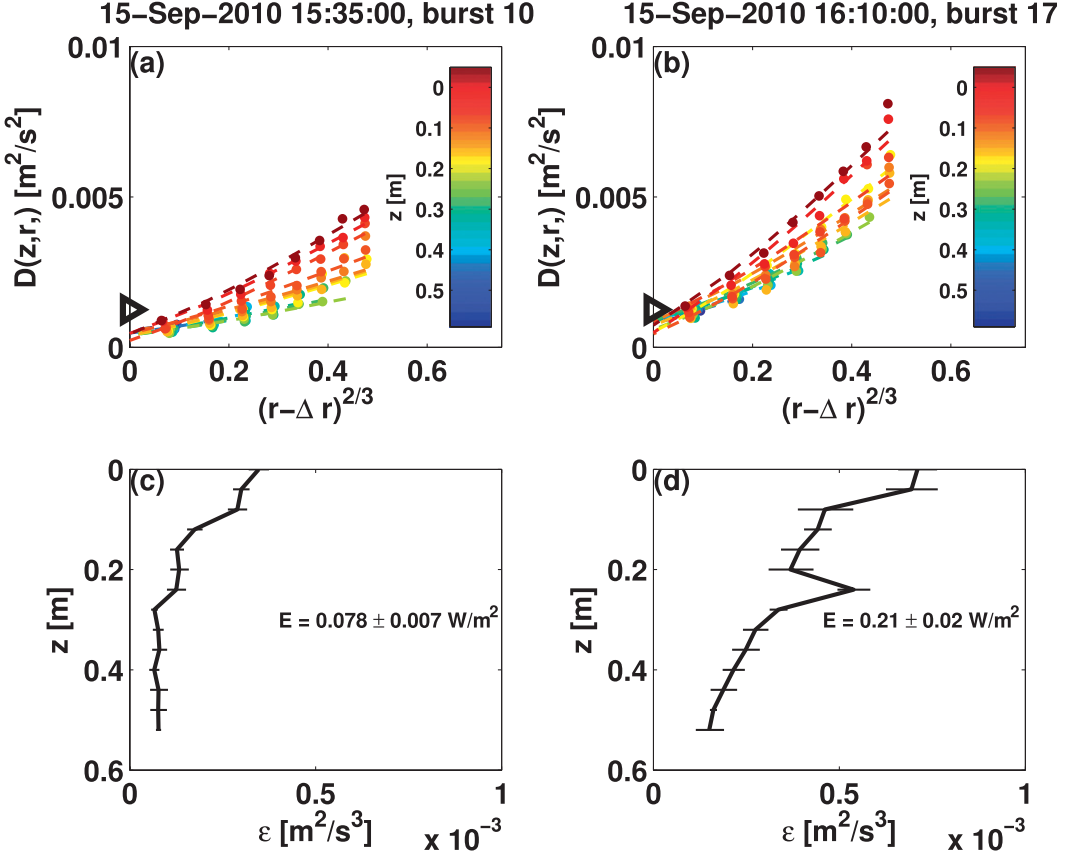


FIG. 6. Example SWIFT burst results from in shallow water at the Duck FFR. (left) Nonbreaking conditions outside of the surf zone, and (right) breaking conditions within the surf zone. (a),(b) Velocity structure functions $D(z, r)$ [Eq. (2), dots] and associated fits $A r^{2/3} + N$ [Eq. (4), lines]. Colors indicate distance beneath the wave-following surface, and the predicted noise intercept $N = 2\sigma_u^2$ is shown on the vertical axis (black triangle). (c),(d) Resulting vertical profiles of dissipation rate $\bar{\epsilon}(z)$, with horizontal bars for uncertainties $\sigma_{\epsilon \pm}$ and the integrated total dissipation $E = \rho_w \int \epsilon dz$ reported in the middle of the panel.

used to assess the motion correction to lag distance Δr [Eq. (3)]. Without correcting lag distances for platform motion the noise intercepts are typically negative (not shown), consistent with the reduction of $D(z, r)$ by partially overlapped bins. With appropriate motion correction, the expectation is for N to be in the range $0 < N < 2\sigma_u^2$ and to depend on the correlation cutoff used in screening raw velocity data.

c. Dissipation rate profiles $\bar{\epsilon}(z)$

Assuming homogenous turbulence and a cascade of isotropic eddies in the inertial subrange (Kolmogorov 1941), the dissipation rate of turbulent kinetic energy scales as $\epsilon \sim u'^2/T \sim u'^3/r$, where T is a time scale given by r/u' . The slope $A(z)$ of the $r^{2/3}$ structure function is related to the dissipation rate by

$$\bar{\epsilon}(z) = C_v^{-3} A(z)^{3/2}, \quad (5)$$

where C_v is a constant equal to 1.45 (Wiles et al. 2006) and the root-mean-square error (RMSE) between the fitted $A(z)r^{2/3}$ and the actual structure $D(z, r)$ is propagated to obtain an uncertainty σ_ϵ . This uncertainty is asymmetric, because of the exponent in Eq. (5), and both upper and lower bounds are propagated as $\sigma_{\epsilon \pm}$. This uncertainty is used for another layer of quality control, in addition to $N \ll Ar^{2/3}$, by requiring that $|\sigma_{\epsilon \pm}| \ll \epsilon$.

Examples of the resulting dissipation rate profiles $\bar{\epsilon}(z)$ are shown in Figs. 6c,d and 7c,d. For each example, the profiles are well resolved and decrease away from the surface at $z = 0$. Dissipation rates are increased during breaking (Figs. 6d and 7d), especially near the surface.

The dissipation rate profile $\bar{\epsilon}(z)$ can be integrated to obtain the total dissipation rate per unit surface area,

$$\dot{E} = \rho_w \int \bar{\epsilon}(z) dz, \quad (6)$$

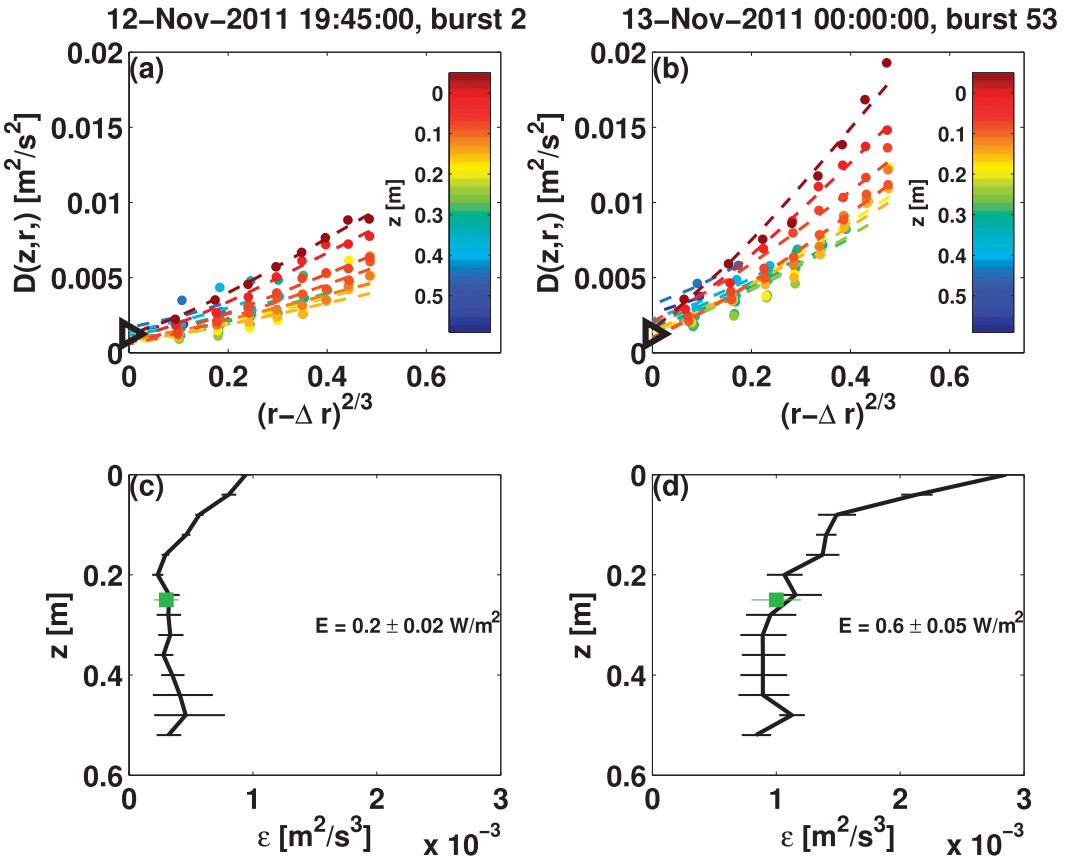


FIG. 7. Example SWIFT burst results from deep water on Lake Washington. (left) Moderate breaking conditions at a short fetch distance, and (right) strong breaking conditions at a larger fetch distance. (a),(b) Velocity structure functions $D(z, r)$ [Eq. (2), dots] and associated fits $Ar^{2/3} + N$ [Eq. (4), lines]. Colors indicate distance beneath the wave-following surface, and the predicted noise intercept $N = 2\sigma_u^2$ is shown on the vertical axis (black triangle). (c),(d) Resulting vertical profiles of dissipation rate $\bar{\epsilon}(z)$, with horizontal bars for uncertainties $\sigma_{\epsilon \pm}$ and the integrated total dissipation $E = \rho_w \int \epsilon dz$ reported in the middle of the panel. The corresponding ADV estimates at $z = 0.25$ m are shown (green).

where ρ_w is the density of water and thus \dot{E} has units of watts per square meter. The depth-integrated dissipation rate \dot{E} in the surf zone example is approximately 2.5 times larger than outside of the surf zone. The depth-integrated dissipation rate \dot{E} in the whitecap example is approximately 3 times larger at long fetch (strong breaking), compared with short fetch (mild breaking).

This integral is limited by the lowest depth ($z \approx 0.5$ m) below the wave-following surface ($z = 0$ m). For some wave conditions, this limitation will be severe given the expectation that the depth-breaking turbulence scales with wave height (Babanin 2011) or water depth (Feddersen 2012). However, for the examples shown, dissipation rates are observed to decrease sharply beneath the wave-following surface, and linear extrapolation below $z = 0.5$ would rarely increase \bar{E} more than 10%. This is consistent with Gemmrich (2010), in which near-surface

profiles of wave-resolved dissipation rates captured the full evolution of breaking turbulence within $z < 0.6$ m. The uncertainties $\sigma_{\epsilon \pm}$ are summed in Eq. (6) to obtain asymmetric uncertainties in the total dissipation $\sigma_{E \pm}$.

Finally, for the Lake Washington deployments, another method to estimate the dissipation rate is incorporated to provide an independent comparison with the structure function method. The second method uses the common approach of rapidly sampled (32 Hz) ADV data to calculate frequency spectra of turbulent kinetic energy (Lumley and Terray 1983; Trowbridge and Elgar 2001; Feddersen 2010). The frequency spectra are converted to wavenumber spectra by assuming the advection of a frozen field (i.e., Taylor's hypothesis), and the dissipation rate is obtained by fitting an amplitude B to the inertial subrange of the spectra $S_{\text{ADV}}(f) = Bf^{-5/3}$, and taking $\bar{\epsilon}_{\text{ADV}} = \rho_w \{B/[(\bar{u}/2\pi)^{2/3} \kappa]\}^{3/2}$. For implementation

on the SWIFT, a Nortek Vector ADV was mounted at $z = 0.25$ m below the surface (see Fig. 1), and the GPS-based drift velocity was used for the advection velocity \bar{u} . The Kolmogorov constant is $k = 0.55$, and the RMSE in the fit is propagated to obtain asymmetric uncertainties on the $\bar{\epsilon}_{\text{ADV}}$ values (similar to the approach for uncertainties in $\bar{\epsilon}$ from the structure function). The ADV method only estimates dissipation at a single depth beneath the surface ($z = 0.25$ m), and thus is insufficient to evaluate the total dissipation [Eq. (6)].

As shown in the example of Fig. 7, and later for all bursts, the estimates from the ADV at $z = 0.25$ m are consistent with structure function estimates at the same depth below the wave-following surface [although it must be noted that the largest values of $\bar{\epsilon}(z)$ are all closer to the surface, and thus are not evaluated by the ADV comparison].

d. Frequency of breaking f_b

The frequency of breaking is the number of waves breaking at a given point per unit time and is a useful quantity in interpreting the dissipation results. Previous work has linked the frequency of breaking to the energetics of breaking, either directly (Banner et al. 2000) or as the first moment of the crest-length distribution by speed $\Lambda(c)$ (Phillips 1985). Video recordings of the surface collected on board the SWIFT are rectified following Holland et al. (1997), such that pixels sizes and locations are corrected for distortion and perspective. After rectification, breaking waves within a $1 \text{ m} \times 1 \text{ m}$ square region immediately in front of the SWIFT are counted manually for each 5-min burst to obtain a burst-averaged frequency of breaking f_b . Restriction to 1 m^2 is consistent with the normalization used in $\Lambda(c)$ studies (e.g., Thomson et al. 2009). Examples of this region are overlaid on the video images in Figs. 2 and 3, and the manually calculated frequencies of breaking are shown. The crest-length distribution by speed $\Lambda(c)$ is not estimated, because the pixel resolution is insufficient over the larger areas needed to observe crest propagation.

4. Results

In this section the methods are applied to all burst data collected during testing, and the results are aggregated to assess spatial patterns, dynamic range, and sensitivity.

a. Surf zone testing

Figure 8 shows cross-shore bathymetry (Fig. 8a) and the aggregated results of all SWIFT bursts on 15 September 2011 (Figs. 8b–d), plotted as a function of cross-shore distance in the local FRF coordination

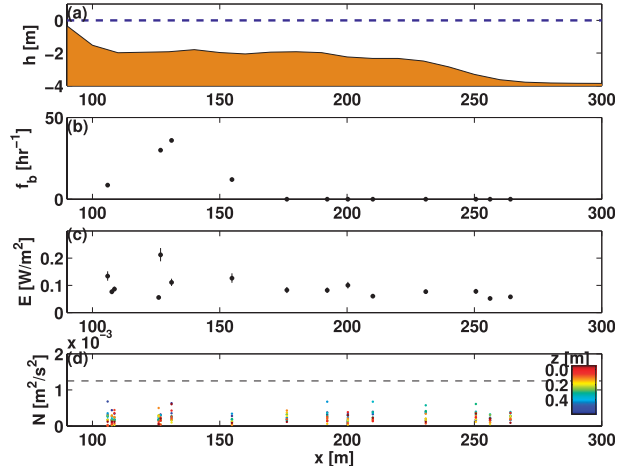


FIG. 8. Aggregated results of SWIFT drifts at the Duck FRF vs cross-shore position. (a) Nearshore bathymetry (shaded region) and the still water level (dashed line). (b) Frequency of breaking calculated from the video images on board the SWIFT. (c) Depth-integrated total dissipation \bar{E} , with vertical bars showing uncertainties $\sigma_{\bar{E}\pm}$. (d) Noise intercept N of the structure function fit, where colors indicate distance beneath the wave-following surface, as in Fig. 6.

system. With small incident waves and a weak (neap) low tide, the surf zone is at approximately $75 < x < 175$ m. (With larger waves and lower tides, the surf zone typically is farther offshore.) The frequency of breaking is maximum in the surf zone ($f_b \sim 40 \text{ hr}^{-1}$ at $x \sim 130$ m in Fig. 8b), as is the vertically integrated total dissipation rate ($\bar{E} \sim 0.2 \text{ W m}^{-2}$ at $x \sim 130$ m in Fig. 8c). Offshore, the frequency of breaking is zero and the total dissipation rates are less than 0.1 W m^{-2} . In contrast, the noise N in the structure function fits does not increase in the surf zone (Fig. 8d), suggesting that noise is correlated with neither the dissipation estimates nor the SWIFT motions (both of which increase in the surf zone). The breaking and dissipation rates likely are biased low by the rapid propagation of the SWIFT through the surf zone. (The SWIFT is visually observed to persist at the break point for only a few waves.)

b. Whitecap testing

Figure 9 shows the aggregated results of all SWIFT bursts on 12 November 2011, plotted as a function of north-south fetch distance x along Lake Washington. Wave heights, as estimated from the SWIFT GPS spectra, increase along the fetch from 0.2 m to 0.9 (Fig. 9a). The frequency of breaking f_b increases along fetch from $\mathcal{O}(10^\circ)$ to $\mathcal{O}(10^2) \text{ h}^{-1}$ (Fig. 9b), and is within the range of previous whitecap observations on Lake Washington (Thomson et al. 2009; Atakturk and Katsaros 1999). The frequency of breaking at larger fetches

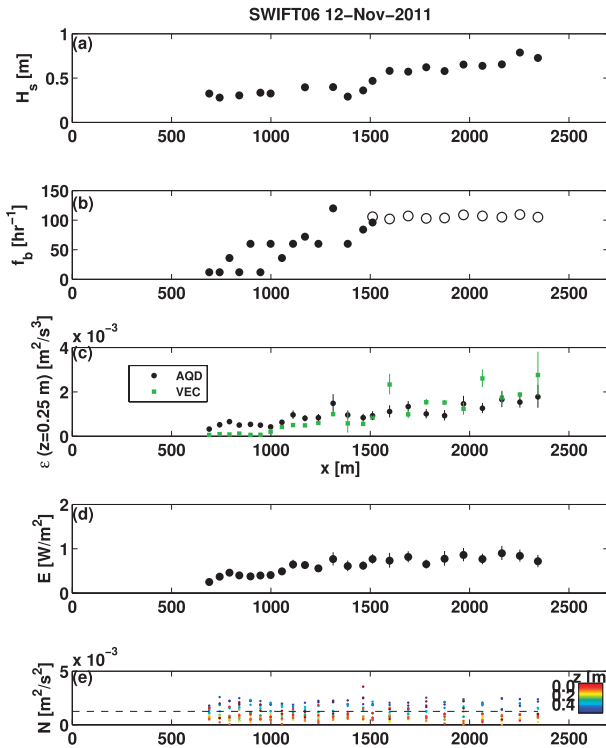


FIG. 9. Aggregated results of SWIFT drifts on Lake Washington vs fetch x . (a) Significant wave height estimated from the SWIFT GPS spectra as $H_s = 4\sqrt{\int S_{\eta\eta}(f) df}$. (b) Breaking rate estimated from the video images on board the SWIFT. (c) The dissipation rate $\bar{\epsilon}(z = 0.25 \text{ m})$ obtained from the Aquadopp structure function (black) compared with the Vector spectra (green), using the relevant level of the profile. (d) Depth-integrated total dissipation \bar{E} , with vertical bars showing uncertainties $\sigma_{E\pm}$. (e) Noise intercept N of the structure function fit, where colors indicate distance beneath the wave-following surface, as in Fig. 7.

($x > 1500 \text{ m}$) is estimated from a second SWIFT nearby and shown with open symbols, because the camera on the primary SWIFT failed. Estimates of dissipation ϵ at $z = 0.25 \text{ m}$ increase along fetch from $\mathcal{O}(10^{-4})$ to $\mathcal{O}(10^{-3}) \text{ m}^2 \text{s}^{-3}$ and are consistent between the AQD structure functions and the VEC inertial spectra (Fig. 9c). The vertically integrated dissipation rate estimates \dot{E} increase along the fetch from 0.1 to 1.0 W m^{-2} (Fig. 9d). In contrast, the noise in the structure function fits does not increase along the fetch (Fig. 9e), which suggests that the noise is correlated with neither the dissipation estimates nor with the SWIFT motions (both of which increase with fetch).

5. Discussion

In this section the magnitude and depth dependence of the dissipation rates during field testing are compared with literature values and simple models. Then, errors and uncertainties in the dissipation rates are discussed,

as well as sensitivity to the correlation cutoff applied to the Doppler velocity measurements.

a. Scaling of dissipation rates

The dissipation rate profiles observed at both the Duck FRF (surf breaking) and on Lake Washington (whitecap breaking) decrease with depth beneath the free surface (i.e., Figs. 6c,d and 7c,d). In the absence of wave breaking (i.e., offshore of the surf zone at the Duck FRF or at very short fetch on Lake Washington), the linear decrease is qualitatively consistent with the well-known wall-layer dependence $\bar{\epsilon}(z) = u_*^3 / (\kappa_v z)$, where u_* is the friction velocity and κ_v is the von Kármán constant, as shown by Agrawal et al. (1992). During breaking, the decrease in dissipation rate with depth is consistent with existing frameworks for wave breaking as a source of turbulence at the surface and turbulent transport as a diffusive processes (e.g., Craig and Banner 1994). At the Duck FRF, the depth dependence is weak, suggesting that transport (or diffusion) is strong and that scaling by depth may be more appropriate (Feddersen 2012). On Lake Washington, the depth dependence is stronger and suggests that wave-breaking turbulence is isolated to within 0.2 m of the surface, consistent with previous observations that whitecap turbulence is largely constrained to a depth less than the wave height (Terray et al. 1996; Gemmrich 2010). This depth scaling will be evaluated further in a future paper, including comparisons with models for the direct injection of wave-breaking turbulence (as opposed to diffusion).

The frequency of breaking and the total dissipation rates observed at the Duck FRF can be compared to a simple budget for the incoming swell. Requiring every incident 10-s period wave to break gives a predicted frequency of breaking $f_b = 0.1 \text{ Hz} = 360 \text{ h}^{-1}$, which is 8 times larger than the $f_b \sim 40 \text{ h}^{-1}$ obtained from the SWIFT in the surf zone (Fig. 8b). Similarly, requiring the energy flux per crest length $F = \rho_w g \sqrt{gh} \int S_{\eta\eta}(f) df$ to be dissipated over a surf zone of cross-shore width x_{sz} , the average dissipation rate per unit surface area is F/x_{sz} (Mei 1989). Using the wave conditions observed at the FRF Aquadopp in $h = 3 \text{ m}$ water depth and $x_{sz} = 100$, the expected average dissipation is 25 W m^{-2} , which is 100 times the total dissipation $\bar{E} \sim 0.2 \text{ W m}^{-2}$ obtained from the SWIFT within the surf zone (Fig. 8c). For both metrics, the discrepancy likely results from the propagation of the SWIFT, which does not stay at the break-point for more than a few waves (as observed from the beach). Previous studies also have estimated surf zone dissipation rates to be much less than the expected energy flux gradient (Trowbridge and Elgar 2001; Bryan et al. 2003; Feddersen 2012). Here, some of the difference

may be explained by dissipation occurring below $z = 0.5$ m, especially near the seabed where Feddersen (2012) finds local dissipation rates in a saturated surf zone as high as 10^{-3} m 2 s $^{-3}$ (i.e., a similar order of magnitude to the near-surface SWIFT values in the Duck FRF surf zone). In addition, during this neap tide and mild waves, many waves did not break until reaching the steep fore-shore ($x \sim 75$ m in Fig. 8), where they are not captured by SWIFT measurements and where wave reflection may account for up to 30% of the incident swell energy flux (Elgar et al. 1994). Finally, energy flux also may be lost to surf zone mean currents (along- and cross shore) and buoyancy (bubble injection).

Related to SWIFT propagation, another significant bias may be the 5-min burst averaging, because the dissipation rates in the surf zone are event driven and unlikely to be normally distributed. Alternate averaging (e.g., lognormal) in Eq. (2) produces similar results for these field tests, suggesting that intermittence cannot be simply treated. The breakpoint of an irregular wave field on a natural beach is not well defined; some waves may break further shoreward and some may break further seaward. Thus, even for a 5-min burst when the SWIFT is drifting within 10 m (cross-shore distance) of the nominal breakpoint, breaking (and presumably maximum dissipation) may only be observed for a few waves. This demonstrates the need for fixed instruments (Eulerian measurements) to interpret the SWIFT estimates. In contrast, whitecapping is more regular, and 5-min burst averages of \bar{E} from SWIFTS and may better able to observe the full dynamic range.

The frequency of breaking and total dissipation rates observed on Lake Washington can be compared to a simple budgets for wind forcing. Under equilibrium conditions (i.e., steady-state, fetch-limited wave field), the frequency of breaking is controlled by the wave steepness at the peak of the spectrum, and the wind input rate W equals the total dissipation rate \dot{E} . Assuming a nearly constant peak period, the frequency of breaking is then expected to be correlated with wave height, as observed in Figs. 9a,b. Assuming forcing of wind waves by a wind stress $\tau = \rho_a C_D U_{10}^2$, where ρ_a is the density of air, U_{10} is the wind speed at a reference height of 10 m, and C_D is a drag coefficient that depends on wave age and wind speed (Donelan et al. 1993), the rate of energy input to the waves is estimated as $W = c_e \tau = c_e \rho_a C_D U_{10}^2$ and is expected to balance the total dissipation \dot{E} . In this formulation, the wind exerts a continuous stress on a surface moving at an effective speed c_e , which is taken as function of the phase speed of the peak waves c_p (Gemmrich et al. 1994; Terray et al. 1996). For the Lake Washington tests with $c_e = c_p$, the wind input is approximately $W \sim 2$ W m $^{-2}$ and is similar to the $\dot{E} \sim 1$ W m $^{-2}$

obtained from the SWIFT measurements. These energy balances will be evaluated further in a future paper, including alternatives to the $W = c_e \tau = c_p \tau$ assumption.

Finally, it must be noted that there are many sources of turbulent dissipation at the air-sea interface. The SWIFT-based estimates are the total dissipation rate in the upper 0.5 m of the ocean, and the above energy budgets attribute all of this dissipation to breaking waves. This assumption is supported by the frequency of breaking measurements, which are well correlated with the dissipation rates. However, to successfully isolate the breaking contribution, it may be necessary to remove a nonbreaking offset, which is estimated a priori, measured independently, or assumed to be the lowest value in the profile.

b. Errors and uncertainty in dissipation rates

There are three interrelated potential sources of error in the dissipation estimates: 1) errors introduced by SWIFT motion, 2) errors in the fit to the spatial structure of an assumed turbulence cascade, and 3) errors in the pulse-coherent Doppler velocity measurements.

Motion contamination is quantified using frequency spectra and corrected with an offset to the lag distances [Eq. (3)] used in the structure function [Eq. (2)]. There are no observed spectral peaks in the difference between velocity bins, although there are SWIFT motion peaks for individual velocity bins (see Figs. 4 and 5). Thus, motion contamination the structure function can be treated as an offset Δr , rather than a wave-dependent quantity.

Errors in the fit to an assumed eddy cascade are quantified by an uncertainty $\sigma_{\epsilon \pm}$, the propagated RMSE of the fit, and by N , the noise intercept of the fit. In general, $\sigma_{\epsilon \pm} \ll \bar{\epsilon}$ and $N \ll A(z)^{2/3}$. More importantly, these values are uncorrelated with changes in wave conditions (Figs. 8d and 9e).

Errors from the pulse-coherent Doppler velocity measurements are more difficult to quantify, although they are implicit to the values of $\sigma_{\epsilon \pm}$ and N discussed above. A threshold for pulse correlation commonly is used to remove spurious points (e.g., Rusello 2009; Feddersen 2010), and the choice of $c > 50$ (out of 100) is evaluated relative to the implicit error N . Figures 10 and 11 show the distributions of N over all bursts and all vertical positions for four different values of correlation cutoffs. Also shown are vertical lines for the predicted $N = 2\sigma_u^2$ given a Doppler velocity uncertainty of $\sigma_u = 0.025$ m s $^{-1}$, or 5% of the along-beam velocity range. The noise intercept N tends to be normally distributed for a given depth z , as expected for white noise. There is a clear trend toward narrower distributions and smaller N values with higher correlation cutoffs, as expected for velocity uncertainty σ_u decreasing with increasing pulse correlation.

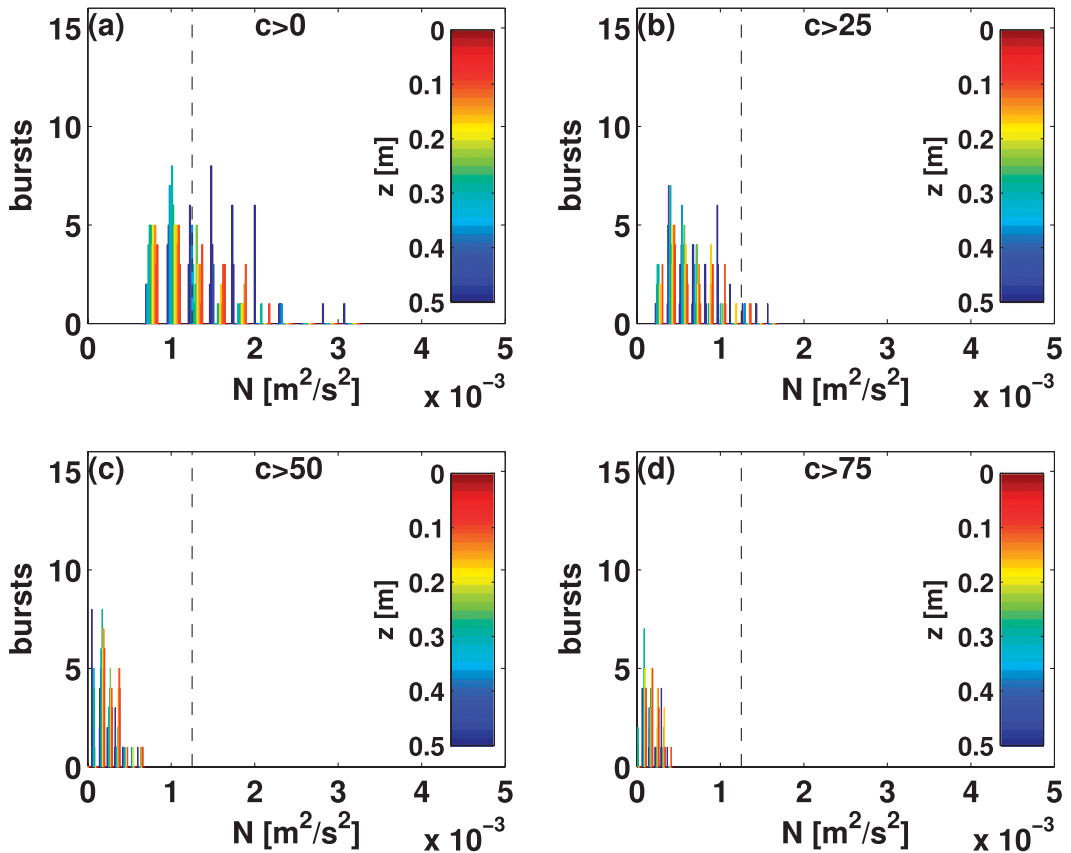


FIG. 10. Distributions of noise intercepts N from all bursts at Duck FFR using four different pulse correlation c cutoffs for quality control of velocity data. (a) $c > 0$, (b) $c > 25$, (c) $c > 50$, and (d) $c > 75$. Colors indicate distance beneath the wave-following surface, as in Fig. 6. Predicted value for N , given a Doppler velocity uncertainty of $\sigma_u = 0.025 \text{ m s}^{-1}$ (dashed lines).

For $c > 50$, the shallow water tests show $N < 2\sigma^2$ for all bursts and all vertical positions (Fig. 10), and the deep water tests show $N < 2\sigma^2$ for the majority of bursts and vertical positions (Fig. 11). The difference between tests may be related to the backscatter amplitude, which is also used in initial quality control (require $a > 30$) and is generally higher in the surf zone. The larger N values on Lake Washington may be the result of peak waves ($f_p = 0.33 \text{ Hz}$) that are closer to the natural frequency of the SWIFT ($f_n = 0.7 \text{ Hz}$) and may cause increased motion contamination relative to the peak waves during the Duck FFR testing ($f_p = 0.1 \text{ Hz}$). Within Lake Washington tests (Fig. 11), there also is a trend of larger noise intercepts N closer to the surface ($z = 0$), again suggesting motion contamination is more significant, because the bias to the structure function is more severe further from the Aquadopp [see Eq. (3)].

Although there is no known parametric dependence or clear empirical value, it is evident from the burst examples (Figs. 2 and 3) and full datasets (Figs. 10 and 11) that a higher correlation cutoff improves the quality

of the dissipation rate estimates, at least within the constraint of removing too many points to obtain robust statistics. Testing selected values suggests that $c > 50$ is reasonable cutoff to give $N < 2\sigma^2$ most of the time. For the SWIFT measurements, evaluation of pulse correlations above 50 may be more important in assessing the potential for surface reflections than in quality controlling individual points. Restated, a random distribution of low correlations will have only a small effect on the determination of dissipation rates, but a concentration of low correlations at particular depth indicates acoustic contamination via surface reflection that may severely deteriorate the quality of dissipation estimates using a structure function method.

Finally, the noise intercepts and uncertainties provide guidance on the minimum values of dissipation that may be obtained from the SWIFT observations. Using the $\sigma = 0.025 \text{ m s}^{-1}$ value, the minimum dissipation rate for $N < Ar^{2/3}$ is $\bar{\epsilon}_{\min} = 3.72 \times 10^{-5} \text{ m}^2 (\text{s}^3)^{-1}$. The minimum depth-integrated dissipation rate is then $\dot{E}_{\min} = 0.0238 \text{ W m}^{-2}$. These minima are admittedly

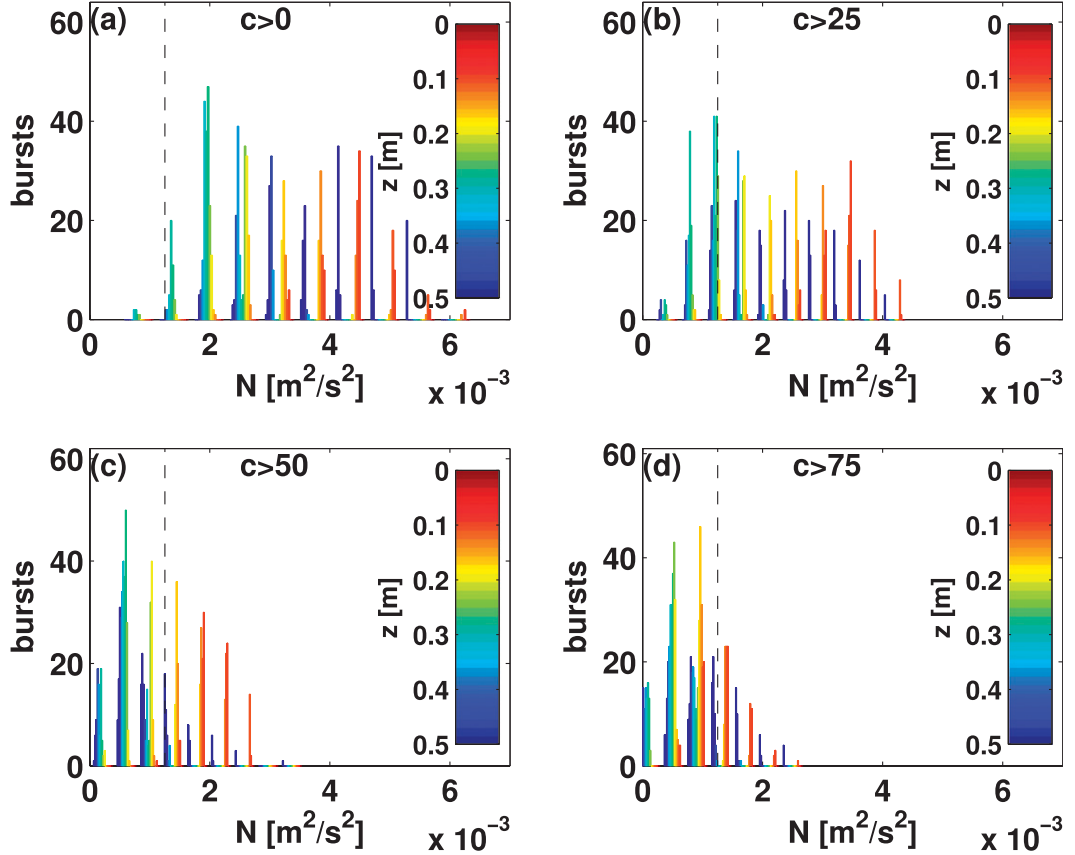


FIG. 11. Distributions of noise intercepts N from all bursts on Lake Washington using four different pulse correlation cutoffs for quality control of velocity data. (a) $c > 0$, (b) $c > 25$, (c) $c > 50$, and (d) $c > 75$. Colors indicate distance beneath the wave-following surface, as in Fig. 7. Expected range for N , given a Doppler velocity uncertainty of $\sigma_u = 0.025 \text{ m s}^{-1}$ (dashed lines).

large in general oceanographic terms; however, they are at least an order of magnitude smaller than any of the results during field tests (or any of the magnitudes estimated from simple analytic energy budgets). In addition, these minima are smaller than the typical uncertainties $\sigma_{\epsilon \pm} \sim 10^{-4} \text{ W m}^{-3}$ and $\sigma_{E \pm} \sim 0.05 \text{ W m}^{-2}$. Clearly, future application of SWIFT-based dissipation rates must be careful to only evaluate results well above these minima and well above the respective uncertainty values.

6. Conclusions

A new wave-following platform, termed the Surface Wave Instrument Float with Tracking (SWIFT), is used to estimate the dissipation rate of turbulent kinetic energy in the reference frame of ocean surface waves. Pulse-coherent Doppler velocity data are used to determine the spatial structure of the near-surface turbulence and thereby estimate burst-averaged dissipation rates as a function of depth and time without assuming the advection of a frozen field (i.e., without using Taylor's

hypothesis). The approach is demonstrated in two field tests under markedly different conditions (shallow water surf breaking versus deep water whitecap breaking). In both cases, motion contamination is successfully minimized and error propagation indicates robust estimates of dissipation. The advantages of the wave-following reference frame, in particular, observations above the still water level and along a spatial gradient (e.g., depth or fetch), are evident in the field tests. Limitations are also evident, in particular the lack of dwell time moving through regions of strong gradients.

Acknowledgments. Thanks to APL-UW Field Engineers J. Talbert and A. deKlerk for tireless efforts in the design, assembling, testing, deployment, and recovery of the SWIFTS. Thanks to the US-ACE Field Research Facility (FRF) staff J. Hanson and K. Hathaway for excellent logistical support, array data, and bathymetry surveys. Thanks to C. Chickadel, D. Clark, M. Haller, D. Honegger, A. Jessup, E. Williams, and G. Wilson for daily shore support during FRF tests, and to

M. Schwendeman for help with Lake Washington tests. Thanks to F. Feddersen, G. Farquharson, J. Gemmrich, G. Gerbi, R. Holman, P. J. Rusello, and anonymous reviewers for many helpful discussions and comments on the manuscript. Funding provided by the National Science Foundation, the Office of Naval Research, and the University of Washington Royalty Research Fund.

REFERENCES

- Agrawal, Y., E. A. Terray, M. A. Donelan, P. A. Hwang, A. J. Williams III, W. M. Drennan, K. Kahma, and S. A. Krtaigorodskii, 1992: Enhanced dissipation of kinetic energy beneath surface waves. *Nature*, **359**, 219–220, doi:10.1038/359219a0.
- Atakturk, S. S., and K. B. Katsaros, 1999: Wind stress and surface waves observed on Lake Washington. *J. Phys. Oceanogr.*, **29**, 633–650.
- Babanin, A. V., 2011: *Breaking and Dissipation of Ocean Surface Waves*. Cambridge University Press, 480 pp.
- Banner, M. L., and D. H. Peregrine, 1993: Wave breaking in deep water. *Annu. Rev. Fluid Mech.*, **25**, 373–397.
- , A. V. Babanin, and I. Young, 2000: Breaking probability for dominant waves on the sea surface. *J. Phys. Oceanogr.*, **30**, 3145–3160.
- Battjes, J., 1988: Surf-zone dynamics. *Annu. Rev. Fluid Mech.*, **20**, 257–293.
- Bryan, K. R., K. P. Black, and R. M. Gorman, 2003: Spectral estimates of dissipation rate within and near the surf zone. *J. Phys. Oceanogr.*, **33**, 979–993.
- Craig, P. D., and M. L. Banner, 1994: Modeling wave-enhanced turbulence in the ocean surface layer. *J. Phys. Oceanogr.*, **24**, 2546–2559.
- Donelan, M., F. W. Dobson, S. D. Smith, and R. J. Anderson, 1993: On the dependence of sea surface roughness on wave development. *J. Phys. Oceanogr.*, **23**, 2143–2149.
- Elgar, S., T. H. C. Herbers, and R. T. Guza, 1994: Reflection of ocean surface waves from a natural beach. *J. Phys. Oceanogr.*, **24**, 1503–1511.
- , B. Raubenheimer, and R. T. Guza, 2001: Current meter performance in the surf zone. *J. Atmos. Oceanic Technol.*, **18**, 1735–1746.
- Feddersen, F., 2010: Quality controlling surf zone acoustic Doppler velocimeter observations to estimate the turbulent dissipation rate. *J. Atmos. Oceanic Technol.*, **27**, 2694–2696.
- , 2012: Observations of the surf-zone turbulent dissipation rate. *J. Phys. Oceanogr.*, **42**, 386–399.
- Gemmrich, J., 2010: Strong turbulence in the wave crest region. *J. Phys. Oceanogr.*, **40**, 583–595.
- , and D. Farmer, 1999: Observations of the scale and occurrence of breaking surface waves. *J. Phys. Oceanogr.*, **29**, 2595–2606.
- , and —, 2004: Near-surface turbulence in the presence of breaking waves. *J. Phys. Oceanogr.*, **34**, 1067–1086.
- , T. Mudge, and V. Polonichko, 1994: On the energy input from wind to surface waves. *J. Phys. Oceanogr.*, **24**, 2413–2417.
- Gerbi, G., J. Trowbridge, E. Terray, A. J. Plueddemann, and T. Kukulka, 2009: Observations of turbulence in the ocean surface boundary layer: Energetics and transport. *J. Phys. Oceanogr.*, **39**, 1077–1096.
- Graber, H., E. Terray, M. Donelan, W. Drennan, J. V. Leer, and D. Peters, 2000: ASIS—A new air-sea interaction spar buoy: Design and performance at sea. *J. Atmos. Oceanic Technol.*, **17**, 708–720.
- Herbers, T. H. C., N. R. Russnogle, and S. Elgar, 2000: Spectral energy balance of breaking waves within the surf zone. *J. Phys. Oceanogr.*, **30**, 2723–2737.
- , P. F. Jessen, T. T. Janssen, D. B. Colbert, and J. H. MacMahan, 2012: Observing ocean surface waves with GPS-tracked buoys. *J. Atmos. Oceanic Technol.*, **29**, 944–959.
- Holland, K. T., R. A. Holman, T. C. Lippmann, J. Stanley, and N. Plant, 1997: Practical use of video imagery in nearshore oceanographic field studies. *IEEE J. Oceanic Eng.*, **22**, 81–92, doi:10.1109/48.557542.
- Kolmogorov, A. N., 1941: Dissipation of energy in the locally isotropic turbulence. *Dokl. Akad. Nauk SSSR*, **30**, 301–305.
- Lumley, J. L., and E. A. Terray, 1983: Kinematics of turbulence convected by a random wave field. *J. Phys. Oceanogr.*, **13**, 2000–2007.
- MacMahan, J., J. Brown, and E. Thornton, 2009: Low-cost handheld GPS for measuring surf-zone currents. *J. Coastal Res.*, **25**, 744–754.
- Mei, C., 1989: *The Applied Dynamics of Ocean Surface Waves*. Advanced Series on Ocean Engineering, Vol. 1, World Scientific, 760 pp.
- Melville, W. K., 1996: The role of surface-wave breaking in air-sea interaction. *Annu. Rev. Fluid Mech.*, **28**, 279–321.
- Middleton, F., L. LeBlanc, and M. Czarnecki, 1977: Spectral tuning and calibration of a wave following buoy. *J. Pet. Tech.*, **29**, 652–653.
- Pascal, R. W., and Coauthors, 2011: A spar buoy for high-frequency wave measurements and detection of wave breaking in the open ocean. *J. Atmos. Oceanic Technol.*, **28**, 590–605.
- Phillips, O. M., 1985: Spectral and statistical properties of the equilibrium range in wind-generated gravity waves. *J. Fluid Mech.*, **156**, 495–531.
- Rusello, P. J., 2009: A practical primer for pulse coherent instruments. Nortek AS Tech. Rep. TN-027, 17 pp. [Available online at <http://www.nortekusa.com/lib/technical-notes/tn-027-pulse-coherent-primer>.]
- , and E. Cowen, 2011: Turbulent dissipation estimates from pulse coherent Doppler instruments. *Proc. IEEE/OES 10th Current, Waves and Turbulence Measurements (CWTM)*, Monterey, CA, IEEE, 167–172.
- Schmidt, W. E., B. T. Woodward, K. S. Milikan, R. T. Guza, B. Raubenheimer, and S. Elgar, 2003: A GPS-tracked surf zone drifter. *J. Atmos. Oceanic Technol.*, **20**, 1069–1075.
- Spydell, M., F. Feddersen, R. T. Guza, and W. E. Schmidt, 2007: Observing surf-zone dispersion with drifters. *J. Phys. Oceanogr.*, **37**, 2920–2939.
- Terray, E., M. Donelan, Y. Agrawal, W. Drennan, K. Kahma, A. Williams, P. Hwang, and S. Kitagorodskii, 1996: Estimates of kinetic energy dissipation under breaking waves. *J. Phys. Oceanogr.*, **26**, 792–807.
- Thomson, J., A. Jessup, and J. Gemmrich, 2009: Energy dissipation and the spectral distribution of whitecaps. *Geophys. Res. Lett.*, **36**, L11601, doi:10.1029/2009GL038201.
- Trowbridge, J., and S. Elgar, 2001: Turbulence measurements in the surf zone. *J. Phys. Oceanogr.*, **31**, 2403–2417.
- Wiles, P. J., T. P. Rippeth, J. H. Simpson, and P. J. Hendricks, 2006: A novel technique for measuring the rate of turbulent dissipation in the marine environment. *Geophys. Res. Lett.*, **33**, L21608, doi:10.1029/2006GL027050.
- Zedel, L., A. Hay, R. Cabrera, and A. Lohrmann, 1996: Performance of a single-beam pulse-to-pulse coherent Doppler profiler. *IEEE J. Oceanic Eng.*, **21**, 290–297.